

CoStructure: Conjoint radiance field optimization for urban scene reconStructure with limited image overlap

Fusang Wang^{1,2} Hala Djeghim^{1,3} Nathan Piasco¹ Moussab Bennehar¹
 Luis Roldão¹ Dzmitry Tsishkou¹
¹Noah’s Ark, Huawei Paris Research Center, France
²CAOR, Mines Paris-PSL, France
³IBISC, Evry Paris-Saclay University, France

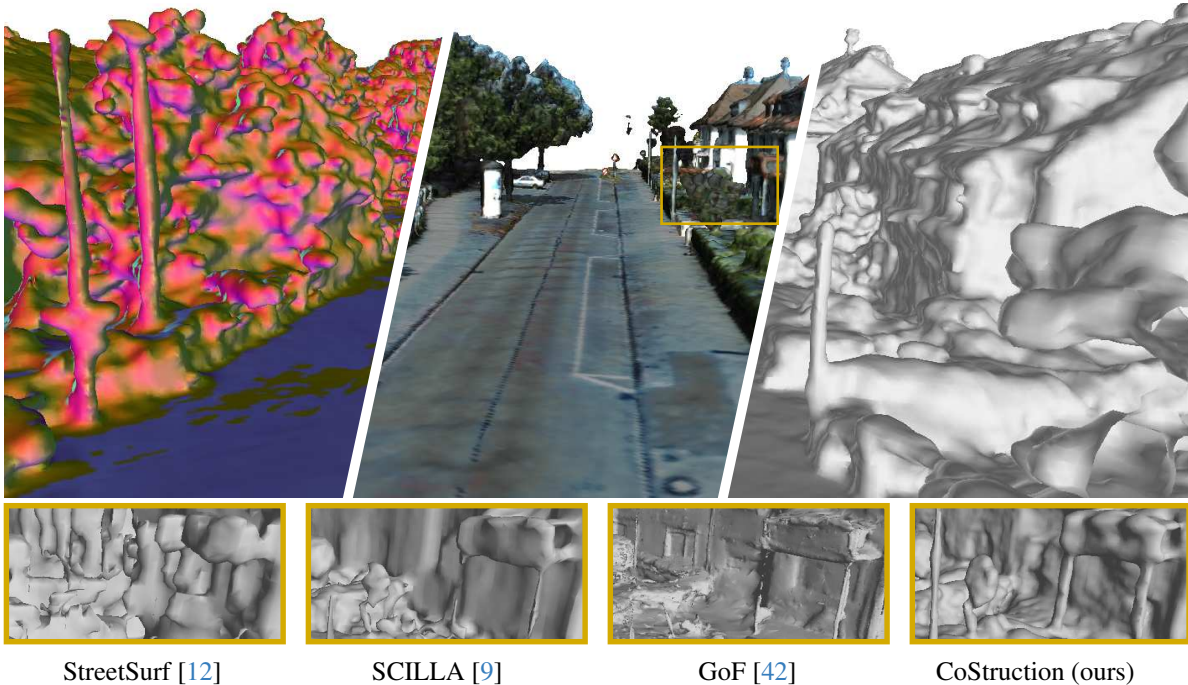


Figure 1. We introduce **CoStructure**, a novel hybrid implicit surface reconstruction method specifically designed for large-scale driving sequences with limited camera overlap. Extensive experiments on four major driving datasets demonstrate the superiority of CoStructure’s mesh (top) over previous state-of-the-art methods (bottom).

Abstract

Reconstructing the surrounding surface geometry from recorded driving sequences poses a significant challenge due to the limited image overlap and complex topology of urban environments. SoTA neural implicit surface reconstruction methods often struggle in such setting, either failing due to small vision overlap or exhibiting suboptimal performance in accurately reconstructing both the surface and fine structures. To address these limitations, we introduce **CoStructure**, a novel hybrid implicit surface reconstruction method tailored for large driving sequences with limited camera overlap. CoStructure leverages cross-representation uncertainty estimation to filter out ambiguous geometry caused by limited observations. Our method

performs joint optimization of both radiance fields in addition to guided sampling achieving accurate reconstruction of large areas along with fine structures in complex urban scenarios. Extensive evaluation on major driving datasets demonstrates the superiority of our approach in reconstructing large driving sequences with limited image overlap, outperforming concurrent SoTA methods.

1. Introduction

Accurate 3D surface reconstruction of large urban scenes is essential for many challenging autonomous driving applications, such as scene relighting [25], simulation, and 3D object insertion [37]. However, achieving high-quality re-

constructions in driving environments remains a significant challenge, where the difficulty primarily stems from two key factors:

- **Complex outdoor geometry:** Urban scenes often feature arbitrary object arrangements, including large textureless planar surfaces and intricate fine structures.
- **Geometric ambiguity:** Limited camera overlap and the linear trajectory of vehicles introduce significant uncertainty in the reconstruction process.

Neural Radiance Fields (NeRF) [21] have emerged as a powerful approach for 3D reconstruction. It represents 3D scenes as a volumetric density field using differentiable volume rendering equations enabling scene reconstruction from images and their associated camera poses. Although NeRF-based methods have demonstrated impressive results in capturing high frequency scene details [1, 23], its under-constrained optimization problem leads to bad scene geometry, especially on planar regions [5, 24]. To adapt to large scene with complex structures, either 3D priors, such as LiDARs, or strong assumptions are introduced to constrain the original optimization problem [8, 26, 31, 32].

Neural implicit surface methods [33, 34, 40], on the other hand, propose to replace the volumetric density field in NeRF with a Signed Distance Function (SDF). The SDF formulation represents the surface at its zero level sets and can be easily regularized using the eikonal constraint. Current neural SDF methods demonstrate high fidelity reconstruction quality in object-centric scenes with large overlap between the training images [17, 35, 41]. However, such formulation fail to reconstruct urban scenes captured by vehicle-mounted cameras due to limited observation overlap and linear sensor trajectory [7, 9].

To achieve high quality surface reconstruction for autonomous driving, recent methods explore a hybrid representation of the volumetric field and SDF field and have demonstrated promising reconstruction results [9, 12], but achieve suboptimal geometry reconstruction due to strong geometric assumptions about the scene topology or coarse and inaccurate initialization from volumetric field.

Following the idea of combining the strength of both representations, we propose to address the aforementioned challenges with **CoStructure**: a conjoint radiance field optimization solution using guided sampling via cross-representation uncertainty estimation. In particular, to address ambiguities in the scene geometry caused by limited camera overlap, we propose cross-representation uncertainty estimation to filter out invalid cues. Furthermore, to handle arbitrary object arrangements with large planar areas and fine structures, we propose to jointly optimize the two radiance fields via guided sampling for efficient rendering and accurate reconstruction. We evaluate our proposed solution on four public driving datasets: KITTI-360 [18], Pan-

daset [39], Waymo Open Dataset [29], and nuScenes [2], demonstrating that our method can accurately reconstructs complex urban geometry with limited image overlap.

The main contributions of our method are the following:

- **joint optimization of a volumetric and an SDF models with cross-supervision** for efficient reconstruction of complex urban scene,
- **a novel guided sampling strategy leveraging cross-representation uncertainty estimation** to filter out ambiguous geometric cues caused by limited overlap between training images,
- **adaptive masked Eikonal constrain** to reduce over-regularization of SDF at early training stages.

2. Related work

Neural implicit surface reconstruction Traditional surface reconstruction techniques, such as Multi-View Stereo (MVS) [22], have long been the cornerstone of 3D reconstruction tasks. However, their multi-step pipelines are prone to error accumulation, often resulting in incomplete or inaccurate reconstructions.

Neural implicit surface reconstruction methods have emerged as a promising solution to address these limitations. These methods primarily adapt volume rendering equations to achieve more accurate surface estimation [33, 40]. Subsequent works have built upon this framework to reduce training times and enhance performance [34] or to improve the fidelity on complex surface reconstruction [17, 35]. Notably, Neuralangelo [17] and Neurodin [35] achieve highly fidelity reconstruction of complex geometries in object-centric scenes where large observation overlaps are present. However, they face significant challenges when applied to autonomous driving scenarios [7, 9], where the camera trajectory is linear and image overlap is limited.

Urban outdoor surface reconstruction. To reconstruct surfaces in outdoor urban scenes for autonomous driving, recent methods often rely on 3D supervision [27, 37] or strong geometric priors [12, 31] to model large planar areas. StreetSurf [12] models different regions—close, far, and sky—using hierarchical space partitioning, 3D and 4D hash grids, and occupancy grids to facilitate efficient ray sampling. However, this approach is limited in applicability, as it imposes strong priors on the initialization of the Signed Distance Field (SDF) based on the vehicle’s ego poses, restricting its use to a narrower set of scenarios.

Recent approaches have also explored 3D Gaussian splatting for surface reconstruction [3, 4, 11]. These methods, however, often rely on heavy post-processing techniques, such as Poisson Surface Reconstruction [15], to extract the final surface, adding computational complexity. Gaussian Opacity Field (GoF) [42] offers a direct approach

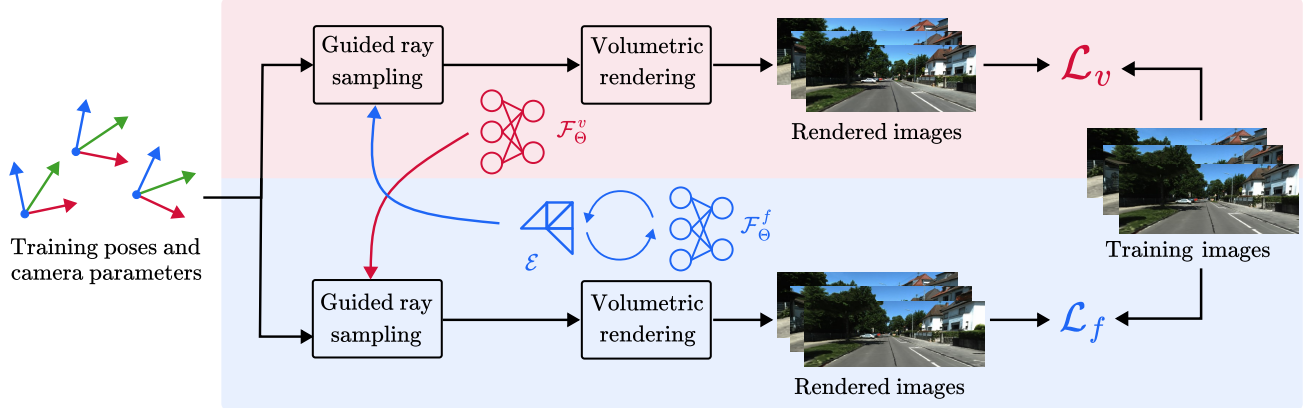


Figure 2. **Overview of CoStructure.**: we jointly train two implicit model: a volumetric representation \mathcal{F}_Θ^v and a SDF \mathcal{F}_Θ^f with a mutual guidance provided through our Guided Ray Sampling strategy. A colored mesh of the scene \mathcal{E} is periodically extracted from the SDF representation.

for mesh extraction by explicitly learning level sets, avoiding the need for post-processing. However, these methods may suffer from excessive memory usage when reconstructing large-scale driving scenes. To address this, StreetSurfGS [7] introduces a planar-based octree representation and segmented training, significantly reducing memory usage and making the method more suitable for large-scale scene reconstruction in autonomous driving.

Hybrid scene representation. Newly developed hybrid approaches have sought to combine volumetric and Signed Distance Field (SDF) representations, aiming to leverage the strengths of both methods [9, 30, 38]. These methods demonstrate that integrating both volumetric and SDF representations can enhance both rendering efficiency and reconstruction accuracy. Specifically, Turki et al. [30] and Wang et al. [38] divide the scene into volumetric and surface regions based on a locally scaled SDF parameter, which is learned through an auxiliary head. They have shown promising results in achieving fast training and efficient rendering, especially for datasets with high overlap and object-centric scenes.

SCILLA [9], on the other hand, introduces a hybrid representation designed for large urban scene reconstruction. It utilizes a volumetric initialization of the signed distance field to progressively guide surface reconstruction, enabling the reconstruction of complex urban scenes with limited visual overlap. However, it still faces challenges in maintaining geometric accuracy, particularly in the reconstruction of fine details.

To address this limitation, we propose an improved approach that better combines the strengths of both representations through conjoint optimization, utilizing guided sampling via cross-representation uncertainty estimation.

3. Method

Given a collection of RGB images of an urban area with limited overlap and captured by sensors mounted on a moving vehicle, our goal is to resolve perspective geometry ambiguities introduced by partial observations of the scene and to reconstruct accurate surface with precise structural details.

3.1. CoStructure joint fields optimization

Overview. We propose to jointly optimize two implicit representations to faithfully and efficiently reconstruct a complex urban scene: a volumetric radiance field \mathcal{F}_Θ^v and an SDF field \mathcal{F}_Θ^f with trainable weights Θ_v and Θ_f , respectively. We also extract at regular intervals during the training process a colored mesh \mathcal{E} from \mathcal{F}_Θ^f using the marching cubes algorithm. An overview of our method is presented in Fig. 2.

We leverage a volumetric representation to achieve fast convergence and accurate fine-structure reconstruction. Indeed, as demonstrated in [9], volumetric radiance fields are both easier and faster to learn compared to SDFs. This is particularly crucial in outdoor urban scenarios, where the images used for reconstruction share small overlap between them, making it challenging to recover detailed scene geometry. To address this, we also jointly train an SDF representation to harness its advantages for precise surface reconstruction through the Eikonal constraint.

To train both representation efficiently, we introduce our main contribution: a Cross-Representation Guided Ray Sampling (GRS, Sec. 3.2). We propose leveraging cross-representation uncertainty estimation to filter out ambiguous information across representations. This uncertainty estimate is used to guide sampling for both representations, enabling precise surface reconstruction while preserving

fine details. In the following paragraphs, we introduce major concept and notation related to our volumetric and SDF representation.

Background - Implicit volumetric representation. A volumetric radiance field is a continuous function \mathcal{F}_θ^v mapping a position and direction pair $(\mathbf{x}, \mathbf{u}) \in \mathbb{R}^3 \times \mathbb{S}^2$ to a volume density $\sigma \in \mathbb{R}^+$ and a color value $\mathbf{c} \in [0, 1]^3$. Mildenhall et al. [21] model this function with a multi layer perceptron (MLP) whose weights θ are optimized to reconstruct a 3D scene given a set of posed images during training.

To render an image and depth from NeRF, volume rendering is applied to alpha-composite the color for each ray, yielding the final pixel color $\hat{C}_v(r) \in \mathbb{R}^3$ and the depth value $\hat{D}_v(r) \in \mathbb{R}$ to be:

$$\hat{C}_v(r) = \sum_{i=1}^N w_i c_i, \quad w_i = T_i \alpha_i, \quad (1)$$

$$\hat{D}_v(r) = \sum_{i=1}^N w_i z_i, \quad w_i = T_i \alpha_i, \quad (2)$$

where $T_i = \prod_{j=1}^{i-1} (1 - \alpha_j)$ is the accumulated transmittance, $\alpha_i \in \mathbb{R}$ the blending factor and z_i is the distance of the sample to the camera center. Here, α_i is computed from the predicted density: $\alpha_i = 1 - \exp(-\sigma_i \delta_i)$, with $\delta_i \in \mathbb{R}$ being the distance between the samples along the ray.

Background - Implicit surface representation. To constraint the optimization for better surface reconstruction, SDF-based approaches represent the scene surfaces as the zero level set of a signed distance function [33, 40]: $S = \{x \in \mathbb{R}^3 | f(x) = 0\}$, where $f(x)$ is the signed distance value at a given position x . To enable volume rendering, the signed distance function f is then transformed into the density σ using sigmoid-shape mapping for alpha compositing..

NeuS [33] adopted a new formulation of the blending factor α :

$$\alpha_i = \max \left(\frac{\Phi_s(f(p_i)) - \Phi_s(f(p_{i+1}))}{\Phi_s(f(p_i))}, 0 \right), \quad (3)$$

where $f(p_i)$ and $f(p_{i+1})$ are signed distance values at section points centered on x_i , $\Phi_s(x)$ the sigmoid function. Such formulation is unbiased in depth estimation, which enables high fidelity surface reconstruction [17].

3.2. Guided ray sampling

Overview. Because both of our representation use volumetric rendering to generate images, we decide to cross-supervise each model within the ray sampling stage with

our Guided Ray Sampling (GRS) strategy. GRS can be divided into four steps: 1) ray generation, 2) per-ray uncertainty computation, 3) ray classification, and 4) ray sampling. Similar to RobustNeRF [28], we use a robust kernel to compute a per-ray uncertainty value. These values are used to compute uncertainty masks $\mathcal{M}_{d,c}$ to filter rays for the subsequent ray sampling step. Below, we describe more in details how uncertainty values are computed and we introduce the GRS applied to the volumetric model and the one used with the SDF representation.

Uncertainty estimation. Due to partial observations in driving setting, each representation has limitations in capturing certain geometric properties to due limited vision overlap. Therefore, detecting uncertain predictions is crucial for determining which representation to trust. To address this, we leverage depth and photometric uncertainty across predictions from \mathcal{F}_Θ^v and \mathcal{F}_Θ^f to identify and filter out noisy predictions.

One intuitive approach to estimate the uncertainty is to compare the expected ray r termination (depth) according to \mathcal{F}_Θ^v , $\hat{D}_v(r)$, and the distance to the first intersection of r with the mesh \mathcal{E} , $\hat{D}_\mathcal{E}(r)$:

$$\mathcal{M}_d(r) = \begin{cases} 1, & \text{if } |1 - \frac{\hat{D}_\mathcal{E}(r)}{\hat{D}_v(r)}| < \tau_d \\ 0, & \text{otherwise} \end{cases} \quad (4)$$

where τ_d is predefined threshold. We introduce a second uncertainty mask, based on a photometric criteria, using the color of the mesh \mathcal{E} associated to ray r , $\hat{C}_\mathcal{E}(r)$, defined as:

$$\mathcal{M}_c(r) = \begin{cases} 1, & \text{if } |\hat{C}_\mathcal{E}(r) - C_{gt}(r)| < \tau_c \\ 0, & \text{otherwise} \end{cases} \quad (5)$$

where $C_{gt}(r)$ is the ground truth RGB values associated to ray r and τ_c is another threshold parameter. The uncertainty mask \mathcal{M}_d provide a measure of the joint convergence of \mathcal{F}_Θ^v and \mathcal{F}_Θ^f while \mathcal{M}_c indicate part of the scene where the SDF representation \mathcal{F}_Θ^f is close to the GT geometry.

GRS for volumetric representation. To improve the volumetric reconstruction on planar surfaces, we guide the volumetric process according to \mathcal{M}_c . The mask \mathcal{M}_c provide a simple yet effective indicator to divide the scenes according to the photometric accuracy of SDF field. Empirically the mask will indicate region with high frequency details and fine structures.

Given a batch of rays $r \in \mathcal{R}_v$ emitted from the camera and $[t_n, t_f]$ be the original sampling interval of a ray r . To guide the sampling of the volumetric representation with the SDF, we adjust the sampling bounds according to $\hat{D}_\mathcal{E}(r)$:

$$[t_n, t_f](r) = \begin{cases} [0, D_{\mathcal{E}}(r) + \delta], & \text{if } \mathcal{M}_c(r) = 0 \\ [0, \infty[, & \text{otherwise} \end{cases} \quad (6)$$

where δ is a hyperparameter (analogous to the shell factor in [38]) periodically updated.

With this formulation, when rays intersect the mesh with a high confidence value, points are sampled near the mesh surface. The rationale behind this approach is that if the color on the mesh surface closely matches the ground truth (GT) color, it is likely that the mesh has converged to the true surface of the scene. In such a case, we can rely on the SDF representation to guide the volumetric representation.

GRS for SDF representation. In contrast to the GRS of \mathcal{F}_{Θ}^v , we leverage the uncertainty mask \mathcal{M}_d to guide the SDF model. Similarly, we modify the near and far plane $[t_n, t_f]$ of ray r according to \mathcal{M}_d :

$$[t_n, t_f](r) = \begin{cases} [D_v(r) - \delta, D_v(r) + \delta], & \text{if } \mathcal{M}_d(r) = 0 \\ [D_{\mathcal{E}}(r) - \delta, D_{\mathcal{E}}(r) + \delta], & \text{otherwise} \end{cases} \quad (7)$$

with δ being the same shell factor hyperparameter described in the previous paragraph.

$\mathcal{M}_d(r)$ indicates regions where the two representations are consistent with each other, suggesting minimal geometric ambiguity. In these regions, we can trust the estimated geometry from both representations and concentrate sampling near the surface. Conversely, it is more subtle to determine which representation to trust in regions where predictions from the two representations are inconsistent. This inconsistency may occur if the volumetric representation fails on large texture-less planes or if the SDF representation fails to reconstruct fine structural details. In such a case, we propose a simple approach: prioritize the volumetric representation and refine any introduced noise through geometric regularization (see Sec. 3.3).

Adaptive thresholding The ray classification step of the guided ray sampling strategy involves choosing thresholds τ_d and τ_c to distinguish between certain and uncertain rays. Selecting such threshold empirically can be complicated as for different scene and reconstruction, this value may change. We propose a simple yet effective adaptive threshold selection method to overcome this limitation. Starting from an initial threshold value, we compute on a regular interval during the reconstruction process the ratio between the number of certain and uncertain rays. We define a scheduling policy that is design to control this ratio along the whole training and we modify the threshold accordingly to meet the ratio requirement. For instance, if the at a certain step of the reconstruction process, the scheduling policy

imposes a ratio of 20% of certain rays and 80% of uncertain rays and the current ratio is 30% of certain rays and 70% of uncertain rays, we will lower the threshold value to reduce the proportion of certain rays.

3.3. Optimization details

Probability sampling. While our GRS modify the sampling boundaries of each ray according to uncertainty masks, we also use a density estimator to further refine the point sampling step. We use a proposal network similar to [9] that is self-supervised by \mathcal{F}_{Θ}^v using the proposal loss \mathcal{L}_p introduced in [1].

Losses. For both representation, \mathcal{F}_{Θ}^v AND \mathcal{F}_{Θ}^f , we use the standard L_1 loss to minimize the pixel-wise color difference between the rendered image \hat{C} , and the ground truth image C , as well as the DSSIM [31] loss on color patches, denoted together as \mathcal{L}_{rgb} . We also apply distortion regularization \mathcal{L}_d introduced in MipNeRF [1] to avoid floaters. Similar to StreetSurf [12], we model the sky color with an auxiliary MLP conditioned on the ray direction and use a sky loss \mathcal{L}_{sky} to constrain the opacity of sky pixels to zero. The segmentation mask is obtained with an off-the-shelf semantic segmentation network [6]. Following SCILLA[9], we supervise the normal associated with the closest sample to the surface with pseudo-ground truth obtained from off-the-shelf network [10] with loss $\mathcal{L}_{\hat{N}}$.

To facilitate more complete fine structure learning, we add an additional semantic head to \mathcal{F}_{Θ}^v and apply an additional cross-entropy loss semantic supervision \mathcal{L}_{rgb} . To constrain our SDF model to respect the eikonal equation, we also apply a masked Eikonal loss \mathcal{L}_{eik} described in the following paragraph to the SDF Field.

The total losses for the volumetric field (\mathcal{L}_v) and the SDF field (\mathcal{L}_f) are:

$$\mathcal{L}_v = \mathcal{L}_{\text{rgb}} + \lambda_d \mathcal{L}_d + \lambda_{\text{sky}} \mathcal{L}_{\text{sky}} + \lambda_{\hat{N}} \mathcal{L}_{\hat{N}} + \lambda_{\text{sem}} \mathcal{L}_{\text{sem}}, \quad (8)$$

$$\mathcal{L}_f = \mathcal{L}_{\text{rgb}} + \lambda_d \mathcal{L}_d + \lambda_{\text{sky}} \mathcal{L}_{\text{sky}} + \lambda_{\hat{N}} \mathcal{L}_{\hat{N}} + \lambda_{\text{eik}} \mathcal{L}_{\text{eik}}^m. \quad (9)$$

where λ_d , λ_{sky} , λ_{normal} , λ_d , λ_{normal} , λ_{eik} are scaling factors.

Adaptive masked Eikonal constrain To facilitate fine structure learning at early stage, we take inspiration from RaNeUS [36] method and relax the eikonal \mathcal{L}_{eik} , together with the normal loss $\mathcal{L}_{\text{normal}}$ with the uncertainty mask \mathcal{M}_d :

$$\mathcal{L}_{\text{eik}}^m = \frac{1}{mn} \sum_{i=1}^m (1 - \mathcal{M}_d(r_i)) \cdot \left(\sum_{j=1}^n (\|\nabla f(x_{(i,j)})\|_2 - 1)^2 \right). \quad (10)$$

Here, $\mathbf{n}_{ij} = \nabla f(x_{(i,j)})$ is the gradient of the sign distance function f of at sample $x_{(i,j)}$. The masked provides two key benefits. Firstly, at each training step, the Eikonal loss is applied only to regions where the SDF field is confident, thereby relaxing constraints on areas with missing

	KITTI-360 [18]								Pandaset [39]							
	Seq. 30		Seq. 31		Seq. 35		Seq. 36		Seq. 23		Seq. 37		Seq. 42		Seq. 43	
	P→M	Prec.	P→M	Prec.	P→M	Prec.	P→M	Prec.	P→M	Prec.	P→M	Prec.	P→M	Prec.	P→M	Prec.
StreetSurf [12]	0.14	0.50	0.09	0.71	<u>0.10</u>	0.67	<u>0.11</u>	0.66	2.52	0.17	0.25	0.66	0.36	0.29	<u>0.19</u>	0.29
SCILLA [9]	<u>0.13</u>	0.56	<u>0.11</u>	0.71	0.11	0.66	0.13	0.72	0.17	<u>0.35</u>	0.22	0.44	0.15	0.59	0.17	0.45
GoF [42] - sparse	–	–	0.29	0.53	0.23	0.63	–	–	0.45	0.32	0.28	0.60	0.28	0.46	0.50	0.35
GoF [42] - dense	0.17	<u>0.71</u>	0.16	<u>0.72</u>	0.20	<u>0.74</u>	<u>0.11</u>	<u>0.80</u>	0.37	<u>0.35</u>	0.27	<u>0.62</u>	0.48	0.33	0.31	0.44
CoStruction (ours)	0.10	0.78	0.09	0.85	0.09	0.84	0.09	0.85	<u>0.21</u>	0.38	<u>0.23</u>	0.53	<u>0.20</u>	0.62	0.20	0.52

	Waymo [29]								nuScenes [2]							
	Seq. 10061		Seq. 13196		Seq. 14869		Seq. 102751		Seq. 0034		Seq. 0071		Seq. 0664		Seq. 0916	
	P→M	Prec.	P→M	Prec.	P→M	Prec.	P→M	Prec.	P→M	Prec.	P→M	Prec.	P→M	Prec.	P→M	Prec.
StreetSurf [12]	<u>0.22</u>	0.43	0.35	0.53	0.23	0.35	0.25	0.24	0.57	<u>0.29</u>	0.78	0.47	0.67	<u>0.50</u>	0.65	0.28
SCILLA [9]	0.19	<u>0.44</u>	0.22	<u>0.48</u>	0.14	<u>0.47</u>	0.19	0.30	<u>0.40</u>	0.20	0.22	0.59	<u>0.40</u>	0.40	<u>0.22</u>	<u>0.54</u>
GoF [42] - sparse	1.87	0.32	2.32	0.20	1.63	0.36	1.54	0.29	1.55	0.07	1.72	0.16	1.49	0.12	1.41	0.18
GoF [42] - dense	1.20	0.38	1.17	0.39	1.55	0.41	2.11	<u>0.34</u>	1.02	0.12	1.55	0.23	1.44	0.12	1.06	0.29
CoStruction (ours)	0.23	0.47	<u>0.27</u>	<u>0.48</u>	<u>0.19</u>	0.60	<u>0.22</u>	0.46	0.30	0.43	<u>0.35</u>	<u>0.56</u>	0.26	0.56	0.21	0.64

Table 1. Quantitative results on KITTI-360 [18], Pandaset [39], Waymo Open Dataset [29] and nuScenes [2]. We report the mean Point to Mesh (P→M) distance in meters m , and the percentage of points with a distance to mesh below $0.15m$ (Prec.). We highlight best performing methods in **green** and second one underlined. Missing entry (–) designate failure case.

structures to facilitate learning. Conversely, to later maintain the properties of a signed distance function, the loss will be applied more broadly once complex structures are captured by the SDF field. This adaptive approach is enabled by the mask calculation, which automatically detects changes in the field’s confidence as training progresses. We also mask the normal loss $\mathcal{L}_{\text{normal}}$ in the same manner to avoid over-regularization at early stage.

SDF refinement. Following Wang et al. [35], we refine the SDF field at the end of the training with this two modifications:

- we enhance the mononormal supervision along with stronger distortion regularization.
- we replace the density estimation provided by the proposal network by computing PDF weight along the ray directly with \mathcal{F}_{Θ}^f .

4. Experiments

Implementation details We use hash encoding to encode the positions [23], and spherical harmonics to encode the viewing directions. We use 2 layers with 64 hidden units for the MLPs \mathcal{F}_{Θ}^h and \mathcal{F}_{Θ}^c . We train our model on a single high-tier GPU using Adam optimizer with a cosine learning rate decay from 10^{-2} to 10^{-4} . The average training time is around 40 mins per scenes. We use Marching Cubes [19] to generate the final mesh that represents the scene. Further implementation details can be found in the supplementary materials.

Datasets We evaluate our method on four public driving datasets: KITTI-360 [18], nuScenes [2], Waymo Open Dataset [29] and Pandaset [39]. We conduct our experiments on four scenes from each dataset with large differences. We

conduct our experiments on static sequences and mask dynamic vehicles for Pandaset scenes.

Baselines We compare our proposed solution to current state-of-the-art (SoTA) surface reconstruction methods, including the SDF-based approaches StreetSurf [12] and SCILLA [9], as well as the Gaussian splatting-based method GoF [42]. StreetSurf [12] models close, far, and sky regions using hierarchical space partitioning, with 3D and 4D hash grids and occupancy grids for efficient ray sampling. SCILLA [9] initializes the SDF field with volumetric density predictions, achieving SoTA results in autonomous driving scenario. GoF [42], a Gaussian splatting method, achieves top performance in object-centric scenes with high image overlap, using 2D Gaussian splatting regularization losses [14], and propose a better mesh extraction solution tailored for 3DGS. We train two variants of GoF: GoF-sparse, initialized from a COLMAP sparse point cloud, and GoF-dense, initialized from a COLMAP dense point cloud.

Evaluation metrics Similar to SCILLA [9], we evaluate the quality of the reconstructed meshes with two metrics:

Point to Mesh (P→M): the mean distances from the ground truth LiDAR points to the predicted SDF-generated mesh.

Precision (Prec.): the percentage of LiDAR points with a distance to the mesh below $0.15m$.

4.1. Results

Quantitative analysis. We report quantitative results across four datasets in Tab. 1. Our method consistently outperforms or matches state-of-the-art approaches, achieving the top metrics in most scenes on KITTI-360 and nuScenes and delivering competitive results on Pandaset and Waymo.



Figure 3. Qualitative experiments results on four popular autonomous driving datasets. Complex scene geometries reconstructed by the mesh are color highlighted. We compare our mesh to the ones from StreetSurf [12], SCILLA [9] and GoF [42]

Averaged over the four datasets, our method achieves a mean $P \rightarrow M$ error of 0.20 m, outperforming SCILLA (0.25 m) and the others. Additionally, we obtain the highest pre-

cision score (0.60), followed by GoF (0.49), demonstrating its strength in capturing precise geometry in regions with consistent geometric cues. This result is aligned with our

	P→M (all)	Prec. (all)	P→M (pole)
w/o guided sampling	0.11	0.79	0.46
w/o masked regu.	0.13	0.75	0.53
w/o proposal sup.	0.09	0.82	0.28
Full model	0.09	0.83	0.21

Table 2. Ablation of our contributions on the KITTI-360 dataset.

conjoint optimization design.

Our performance on Pandaset and Waymo datasets is comparatively lower. This is likely due to the significant occlusions caused by vegetation and trees, which are abundant in this dataset. Given our guided sampling approach, our method is sensitive to heavily occluded objects, leading to reduced accuracy in such scenes.

However on high-quality image datasets like KITTI-360 with little occlusion, our method achieves sub-decimal accuracy on the average Point-to-Mesh (P→M) metric, with a precision of 0.83. This result highlights the effectiveness of our cross-representation uncertainty-guided sampling strategy, particularly when strong alignment exists between the volumetric and SDF representations.

Qualitative analysis. To complete our evaluation, we further present qualitative results in Fig. 3 across different dataset with complex scenes geometry, including a mixture of large road surfaces and fine structures such as poles, traffic lights, and tree trunks..

Both SCILLA [9] and StreetSurf [12] are able to reconstruct smooth complete surface but result in incomplete fine structure reconstruction. GoF [42] produce high quality on fine structures but fails large road plane reconstruction (Nuscenes 0064). Our results demonstrate that our method outperforms others in accurately reconstructing both surfaces and fine structures, under conditions of limited image overlap.

4.2. Ablation study

To have a clear understanding the contribution of each key component in our method, we conducted an ablation study on guided sampling directed by \mathcal{M}_c , masked regularization using \mathcal{M}_c and proposal guidance during early stage. Quantitative and qualitative results from KITTI-360 dataset are shown in Tab. 2 and Fig. 4.

First, we observe that guided sampling significantly improves overall geometry, enhancing both surface accuracy and fine structural details. This is shown by metrics for the entire scene and specifically for thin structures, such as poles, as well as in the visual quality of fine details shown in Fig. 4. These results indicate that guided sampling, enabled by cross-representation uncertainty masks \mathcal{M}_d and \mathcal{M}_c effectively filter ambiguity under limited image overlap condition, leading to more accurate reconstructions.

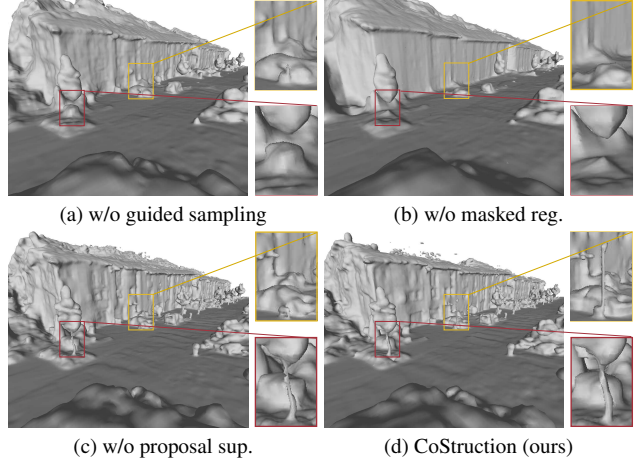


Figure 4. Ablations study: we deactivate some CoStructure’s key components. (a) without guided ray sampling directed by $\mathcal{M}_{d,c}$ (b) without masking \mathcal{L}_{eik} and \mathcal{L}_{normal} with \mathcal{M}_c (c) without proposal guidance for SDF initialization .

Second, the masked regularization with \mathcal{M}_c is for retaining fine structures while ensuring accurate surface geometry. This component significantly improves fine structures reconstruction (from 0.53 to 0.21 P→M metric on poles) while preserving smooth and accurate surfaces.

Lastly, proposal supervision in the initial training stage aids in completing thin structures by providing a stable foundation for complex details that are challenging to reconstruct.

Together, these components enable our method to achieve high-fidelity reconstructions in complex urban scenes with limited image overlap.

5. Conclusion

In this work, we presented **CoStructure**, a hybrid solution with conjoint radiance field optimization designed to reconstruct accurate geometry for complex urban scenes with limited view overlap. We introduced Guided Ray Sampling, directed by cross-representation uncertainty, to filter geometric ambiguities arising from partial observations and achieve precise geometry reconstruction in outdoor environments. Extensive quantitative and qualitative evaluations show that CoStructure outperforms state-of-the-art SDF and Gaussian splatting methods, delivering more accurate reconstructions on both large planar regions and fine structures under autonomous driving setting.

CoStruction: Conjoint radiance field optimization for urban scene reconStruction with limited image overlap

Supplementary Material

6. Additional implementation details

Model architecture. For both representations \mathcal{F}_Θ^v and \mathcal{F}_Θ^f , we use a hash grid for positional embedding [23] and spherical harmonics for directional embedding [16]. Additionally, we adopt the same appearance embedding from NeRF-W [20] to address illumination changes. Both representations utilize independent hash grids, trained separately during the training process, with identical parameters as summarized in Table 3. We also employ two additional density estimators (proposal networks), $\mathcal{F}_\Theta^{p_0}$ and $\mathcal{F}_\Theta^{p_1}$ [1], which are supervised only by the weight estimated by \mathcal{F}_Θ^v , but will be used to guide the sampling for \mathcal{F}_Θ^f during initialization.

The sampling parameters used for training in our experiments are detailed in Table 4. In the refinement stage of the SDF, we replace the estimated densities provided by the proposal networks $\mathcal{F}_\Theta^{p_i}, i \in \{0, 1\}$ with PDF weights computed directly using \mathcal{F}_Θ^f . Additionally, we slightly increase the number of samples for both coarse and fine sampling, setting them to 32 and 28, respectively, to improve the accuracy of density estimation during the refinement stage.

Optimization. The losses we use in CoStruction to optimize the volumetric (\mathcal{L}_v) and SDF fields (\mathcal{L}_f) are:

$$\mathcal{L}_v = \mathcal{L}_{\text{rgb}} + \lambda_d \mathcal{L}_d + \lambda_{\text{sky}} \mathcal{L}_{\text{sky}} + \lambda_{\hat{N}} \mathcal{L}_{\hat{N}} + \lambda_{\text{sem}} \mathcal{L}_{\text{sem}}^m, \quad (11)$$

$$\mathcal{L}_f = \mathcal{L}_{\text{rgb}} + \lambda_d \mathcal{L}_d + \lambda_{\text{sky}} \mathcal{L}_{\text{sky}} + \lambda_{\hat{N}} \mathcal{L}_{\hat{N}} + \lambda_{\text{eik}} \mathcal{L}_{\text{eik}}^m. \quad (12)$$

We set $\lambda_{\text{sky}} = 0.01$, $\lambda_d = 0.001$, $\lambda_{\hat{N}} = 0.01$, $\lambda_{\text{sem}} = 0.001$ and $\lambda_{\text{eik}} = 0.1$. During the SDF refinement stage, we increase $\lambda_{\hat{N}}$ to 0.05 only on flat semantic classes and λ_d to 0.1.

For Pandaset, we reduce the Eikonal loss coefficient to 0.01 during the early stage to facilitate mesh reconstruction, and then restore it to 0.1 for the final two epochs. To improve initialization on large texture-less road planes in the volumetric representation, we activate the total variation

Parameter	Value
Table size	2^{19}
Finest resolution	2048
Coarsest resolution	16
Number of level	16

Table 3. Hash Grid encoding parameters for both volumetric representation and SDF representation

Model	Num. of Sampling
$\mathcal{F}_\Theta^{p_0}$	128
$\mathcal{F}_\Theta^{p_1}$	96
\mathcal{F}_Θ^v	48
\mathcal{F}_Θ^f	24

Table 4. Sampling parameters at Training

regularization on depth prediction during the first epoch for sequences 0034 and 0664 in nuScenes, and sequence 023 in Pandaset, with a weight of $1e-4$.

Datasets. For all experiments, we use the poses provided by the datasets, except Waymo, where inaccuracies in the data required recalculating the vehicle trajectory and sensor calibration using MOISST [13]. The KITTI-360 [18] sequence splits used in our evaluations are summarized in Table 5. For KITTI-360 [18], we use all four cameras, while for Pandaset [39], nuScenes [2], and Waymo Open Dataset [29], we use the three front-facing cameras. Additionally, we sample one image out of every two for KITTI-360 and one image out of every eight for the other datasets.

7. Additional details on Uncertainty Mask

One of our key contributions is to use \mathcal{M}_c to adaptively direct the looseness of the Eikonal constraint on high frequency details and fine structures at early training stages (see our ablation study Sec. 4.2). Fig. 7 shows an example of how such a mask empirically helps divide the scene and how it evolves during training. The black areas in the mask primarily correspond to high-frequency details in the scene, such as fine structures or vegetation, while the white areas represent surface regions such as roads and buildings.

In the initial stage, \mathcal{L}_{eik} is applied mainly to regions with strong "surfacedness", such as roads and buildings. By the

Seq.	KITTI Sync.	Start	End	# frames per cam.
30	0004	1728	1822	48
31	0009	2890	2996	54
35	0009	980	1092	57
36	0010	112	166	28

Table 5. Selected KITTI-360 sequences

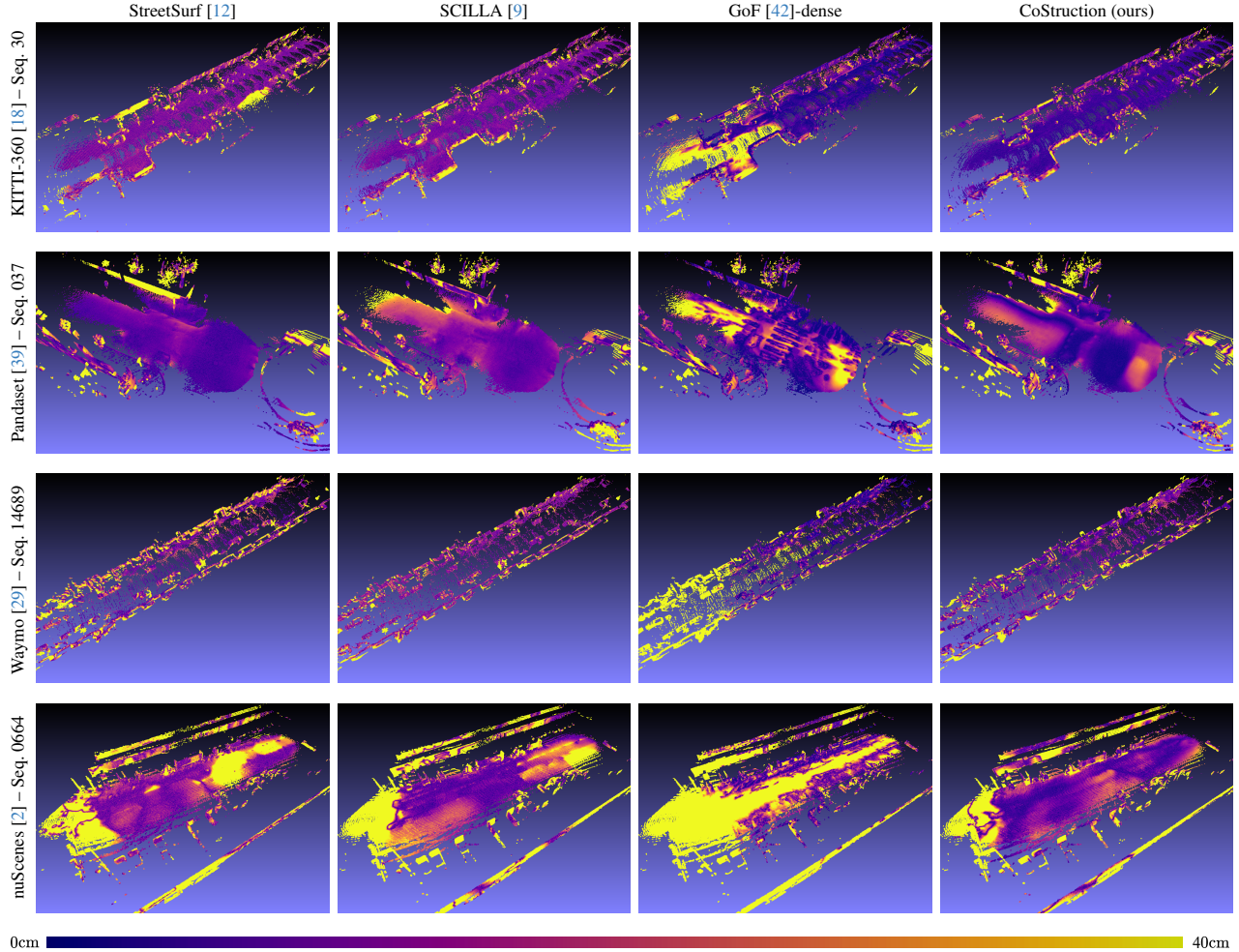


Figure 5. Point-cloud colored by P→M error on sequences reported in Tab 3. We compare our results to the ones from StreetSurf [12], SCILLA [9] and GoF [42]

end of the initialization stage, most surface regions are identified by the mask and constrained by the Eikonal loss. During the refinement stage, as the SDF learns to capture fine structures and predict consistent mesh colors, the Eikonal loss is progressively applied to these regions as well, ensuring adherence to the properties of a signed distance function.

8. Additional experiment results

To provide a more comprehensive evaluation of the geometry throughout the scene, we include LiDAR point cloud visualizations colored by the P→M distance in Fig. 5. The results shown are the same sequences reported in Fig. 3. In the visualization, the color transitions from purple to yellow, indicating errors ranging from 0 cm to 40 cm. Overall, our method exhibits a larger proportion of purple regions and a reduced presence of yellow. Together, these results

indicate that our approach achieves lower reconstruction errors across the entire scene, capturing both large surfaces and fine structures with higher accuracy. Moreover, to provide a more thorough and detailed evaluation compared to other methods, we include additional qualitative comparisons in Fig. 6. These visualizations further demonstrate the reconstruction quality of our approach, particularly in handling complex geometries and fine details.

9. Limitations

Although our method results in overall high mesh quality on both large surfaces and fine structures, it still struggles in certain cases to deliver high-quality reconstructions. These challenges are particularly apparent with extremely fine and repetitive structures (*e.g.*, iron railings), or when such structures are located in heavily occluded environments (*e.g.*, areas surrounded by dense trees). Possible reasons include

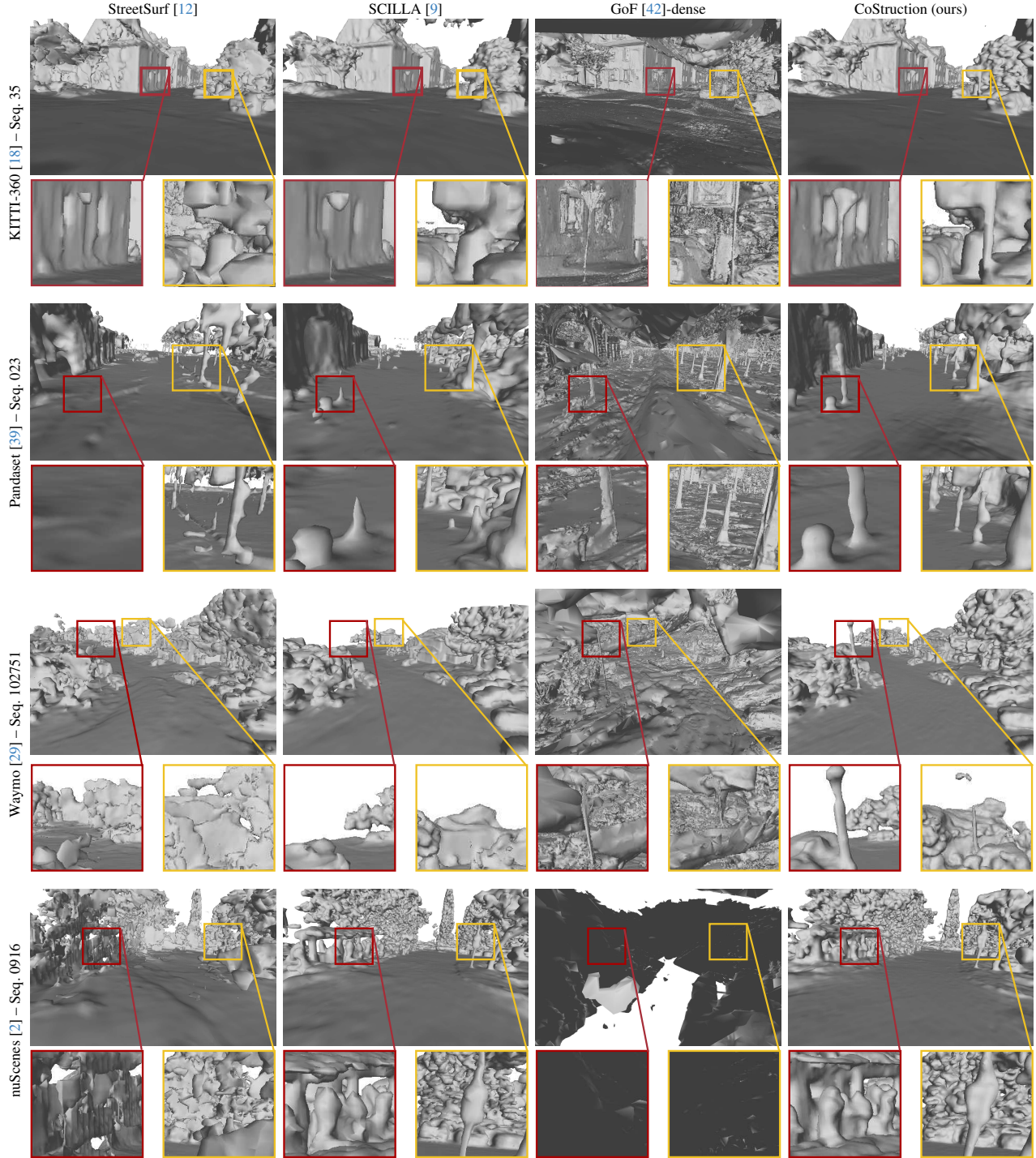


Figure 6. Additional qualitative results highlighting complex geometries. We compare our mesh to the ones generated from StreetSurf [12], SCILLA [9] and GoF [42]

the inability of both representations to produce valid predictions in these scenarios and the guided sampling focusing on incorrect surfaces.

Interestingly, since 3D Gaussians are a more flexible and less constrained representation compared to SDF, GoF [42] performs better at capturing fine structures in such cases,

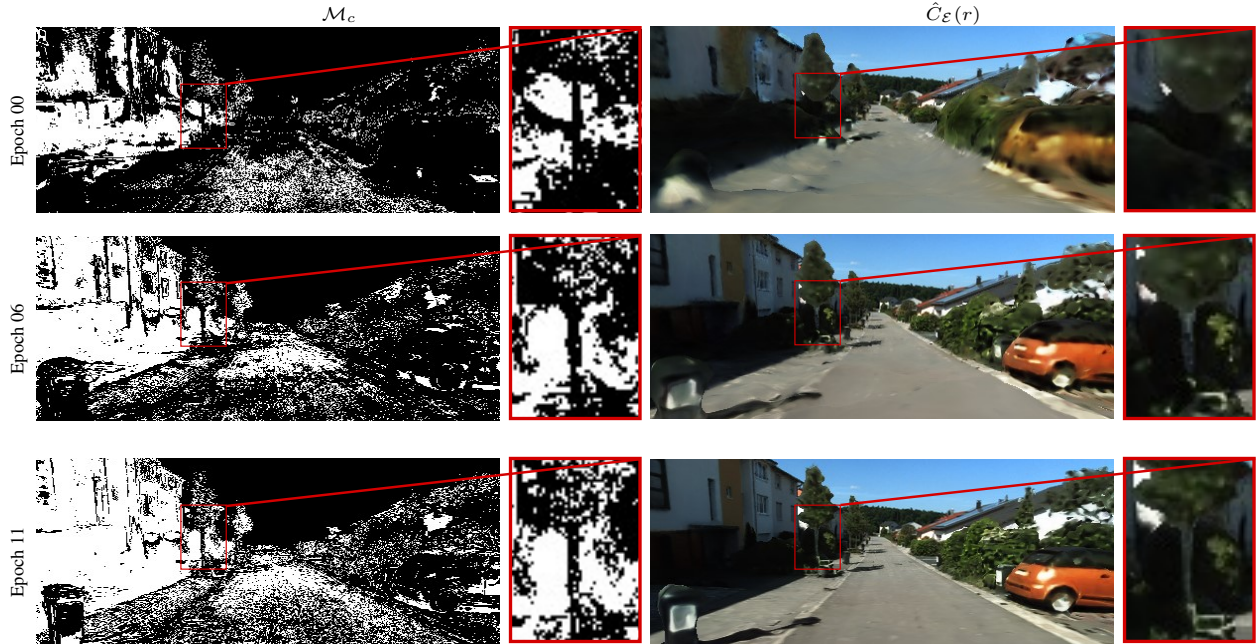


Figure 7. An example of how \mathcal{M}_c , deduced from the mesh color prediction $\hat{C}_\varepsilon(r)$ evolves during the training stage on the KITTI-360 dataset. Where black indicates region where \mathcal{L}_{cik} and $\mathcal{L}_{\text{normal}}$ are loosened during initialization.

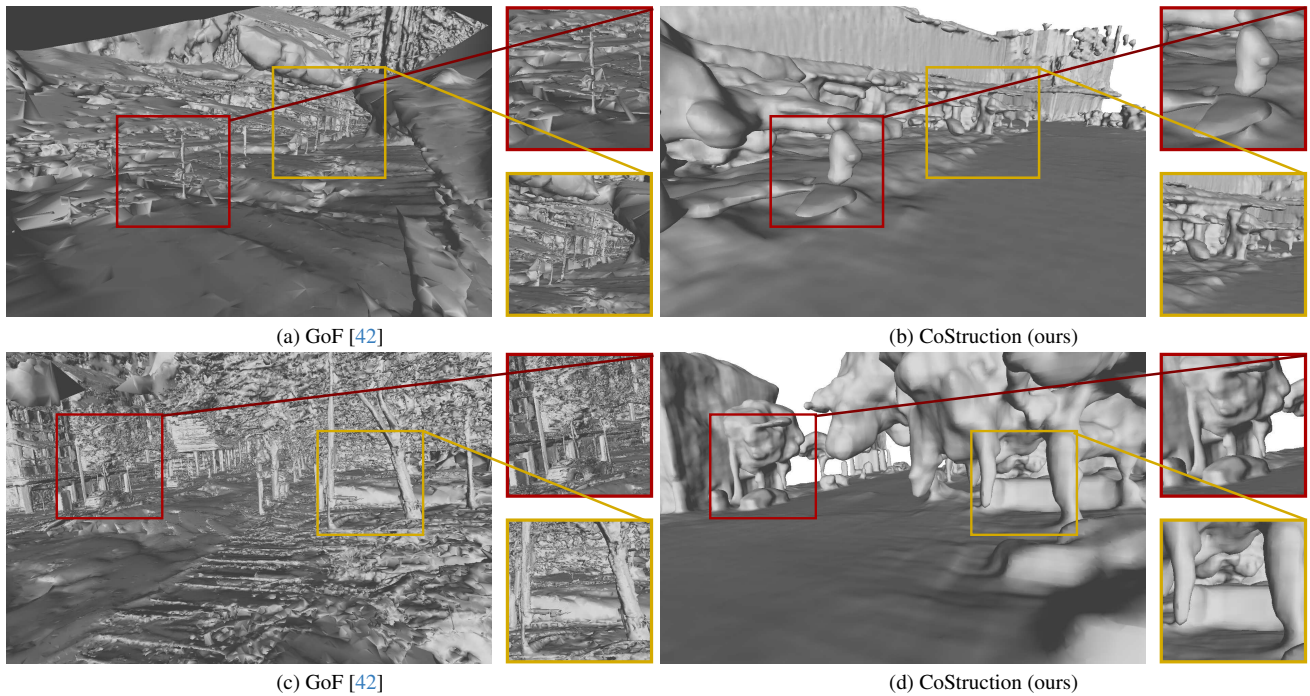


Figure 8. Examples of challenging scenarios. Iron railings from the nuScenes sequence 0072 (top) and dense vegetation occlusion from the Pandaset sequence 043 (bottom).

even though it fails at large surface reconstruction under conditions of limited overlap. Applying our key concept of "co-joint" optimization with uncertainty filtering to rep-

resentations like GoF could be a promising direction for future exploration. We illustrate such cases in Fig. 8.

References

- [1] Jonathan T. Barron, Ben Mildenhall, Dor Verbin, Pratul P. Srinivasan, and Peter Hedman. Mip-nerf 360: Unbounded anti-aliased neural radiance fields. In *CVPR*, 2022. 2, 5, 1
- [2] Holger Caesar, Varun Bankiti, Alex H. Lang, Sourabh Vora, Venice Erin Liong, Qiang Xu, Anush Krishnan, Yu Pan, Giancarlo Baldan, and Oscar Beijbom. nuscenes: A multi-modal dataset for autonomous driving. In *CVPR*, 2020. 2, 6, 7, 1, 3
- [3] Danpeng Chen, Hai Li, Weicai Ye, Yifan Wang, Weijian Xie, Shangjin Zhai, Nan Wang, Haomin Liu, Hujun Bao, and Guofeng Zhang. Pgsr: Planar-based gaussian splatting for efficient and high-fidelity surface reconstruction, 2024. 2
- [4] Hanlin Chen, Chen Li, and Gim Hee Lee. Neusg: Neural implicit surface reconstruction with 3d gaussian splatting guidance, 2023. 2
- [5] Zheng Chen, Chen Wang, Yuan-Chen Guo, and Song-Hai Zhang. Structnerf: Neural radiance fields for indoor scenes with structural hints, 2022. 2
- [6] Bowen Cheng, Ishan Misra, Alexander G. Schwing, Alexander Kirillov, and Rohit Girdhar. Masked-attention mask transformer for universal image segmentation. In *CVPR*, 2022. 5
- [7] Xiao Cui, Weicai Ye, Yifan Wang, Guofeng Zhang, Wengang Zhou, and Houqiang Li. Streetsurfgs: Scalable urban street surface reconstruction with planar-based gaussian splatting, 2024. 2, 3
- [8] Kangle Deng, Andrew Liu, Jun-Yan Zhu, and Deva Ramanan. Depth-supervised nerf: Fewer views and faster training for free. In *Proceedings of the IEEE/CVF Conference on Computer Vision and Pattern Recognition*, pages 12882–12891, 2022. 2
- [9] Hala Djeghim, Nathan Piasco, Moussab Bennehar, Luis Roldão, Dzmitry Tsishkou, and Désiré Sidibé. Scilla: Surface implicit learning for large urban area, a volumetric hybrid solution, 2024. 1, 2, 3, 5, 6, 7, 8
- [10] Ainaz Eftekhari, Alexander Sax, Jitendra Malik, and Amir Zamir. Omnidata: A scalable pipeline for making multi-task mid-level vision datasets from 3d scans. In *ICCV*, 2021. 5
- [11] Antoine Guédon and Vincent Lepetit. Sugar: Surface-aligned gaussian splatting for efficient 3d mesh reconstruction and high-quality mesh rendering. In *CVPR*, 2024. 2
- [12] Jianfei Guo, Nianchen Deng, Xinyang Li, Yeqi Bai, Botian Shi, Chiyu Wang, Chenjing Ding, Dongliang Wang, and Yikang Li. Streetsurf: Extending multi-view implicit surface reconstruction to street views, 2023. 1, 2, 5, 6, 7, 8, 3
- [13] Quentin Herau, Nathan Piasco, Moussab Bennehar, Luis Roldão, Dzmitry Tsishkou, Cyrille Migniot, Pascal Vasseur, and Cédric Demonceaux. Moisst: Multimodal optimization of implicit scene for spatiotemporal calibration. In *IROS*. IEEE, 2023. 1
- [14] Binbin Huang, Zehao Yu, Anpei Chen, Andreas Geiger, and Shenghua Gao. 2d gaussian splatting for geometrically accurate radiance fields. In *ACM SIGGRAPH 2024 Conference Papers*, pages 1–11, 2024. 6
- [15] Michael Kazhdan, Matthew Bolitho, and Hugues Hoppe. Poisson surface reconstruction. In *Eurographics Symp. Geometry Processing*, page 61–70, 2006. 2
- [16] Bernhard Kerbl, Georgios Kopanas, Thomas Leimkühler, and George Drettakis. 3d gaussian splatting for real-time radiance field rendering. *ACM Transactions on Graphics*, 42(4), 2023. 1
- [17] Zhaoshuo Li, Thomas Müller, Alex Evans, Russell H Taylor, Mathias Unberath, Ming-Yu Liu, and Chen-Hsuan Lin. Neuralangelo: High-fidelity neural surface reconstruction. In *CVPR*, 2023. 2, 4
- [18] Yiyi Liao, Jun Xie, and Andreas Geiger. KITTI-360: A novel dataset and benchmarks for urban scene understanding in 2d and 3d. *PAMI*, 2022. 2, 6, 7, 1, 3
- [19] William E. Lorensen and Harvey E. Cline. Marching cubes: A high resolution 3d surface construction algorithm. 21(4), 1987. 6
- [20] Ricardo Martin-Brualla, Noha Radwan, Mehdi SM Sajjadi, Jonathan T Barron, Alexey Dosovitskiy, and Daniel Duckworth. Nerf in the wild: Neural radiance fields for unconstrained photo collections. In *Proceedings of the IEEE/CVF conference on computer vision and pattern recognition*, pages 7210–7219, 2021. 1
- [21] Ben Mildenhall, Pratul P. Srinivasan, Matthew Tancik, Jonathan T. Barron, Ravi Ramamoorthi, and Ren Ng. Nerf: Representing scenes as neural radiance fields for view synthesis. In *ECCV*, 2020. 2, 4
- [22] Pierre Moulon, Pascal Monasse, Romuald Perrot, and Renaud Marlet. OpenMVG: Open multiple view geometry. In *International Workshop on Reproducible Research in Pattern Recognition*, pages 60–74. Springer, 2016. 2
- [23] Thomas Müller, Alex Evans, Christoph Schied, and Alexander Keller. Instant neural graphics primitives with a multiresolution hash encoding. *ACM Trans. Graph.*, 41(4):102:1–102:15, 2022. 2, 6, 1
- [24] Michael Niemeyer, Jonathan T Barron, Ben Mildenhall, Mehdi SM Sajjadi, Andreas Geiger, and Noha Radwan. Regnerf: Regularizing neural radiance fields for view synthesis from sparse inputs. In *Proceedings of the IEEE/CVF Conference on Computer Vision and Pattern Recognition*, pages 5480–5490, 2022. 2
- [25] Ava Pun, Gary Sun, Jingkang Wang, Yun Chen, Ze Yang, Sivabalan Manivasagam, Wei-Chiu Ma, and Raquel Urtasun. Lightsim: Neural lighting simulation for urban scenes, 2023. 1
- [26] Konstantinos Rematas, Andrew Liu, Pratul P Srinivasan, Jonathan T Barron, Andrea Tagliasacchi, Thomas Funkhouser, and Vittorio Ferrari. Urban radiance fields. In *Proceedings of the IEEE/CVF Conference on Computer Vision and Pattern Recognition*, pages 12932–12942, 2022. 2
- [27] Konstantinos Rematas, Andrew Liu, Pratul P. Srinivasan, Jonathan T. Barron, Andrea Tagliasacchi, Tom Funkhouser, and Vittorio Ferrari. Urban radiance fields. In *CVPR*, 2022. 2
- [28] Sara Sabour, Suhani Vora, Daniel Duckworth, Ivan Krasin, David J Fleet, and Andrea Tagliasacchi. Robustnerf: Ignoring distractors with robust losses. In *Proceedings of the IEEE/CVF Conference on Computer Vision and Pattern Recognition*, pages 20626–20636, 2023. 4

- [29] Pei Sun, Henrik Kretzschmar, Xerxes Dotiwalla, Aurelien Chouard, Vijaysai Patnaik, Paul Tsui, James Guo, Yin Zhou, Yuning Chai, Benjamin Caine, Vijay Vasudevan, Wei Han, Jiquan Ngiam, Hang Zhao, Aleksei Timofeev, Scott Ettinger, Maxim Krivokon, Amy Gao, Aditya Joshi, Yu Zhang, Jonathon Shlens, Zhifeng Chen, and Dragomir Anguelov. Scalability in perception for autonomous driving: Waymo open dataset. In *CVPR*, 2020. 2, 6, 7, 1, 3
- [30] Haithem Turki, Vasu Agrawal, Samuel Rota Bulò, Lorenzo Porzi, Peter Kotschieder, Deva Ramanan, Michael Zollhöfer, and Christian Richardt. Hybridnerf: Efficient neural rendering via adaptive volumetric surfaces. In *Proceedings of the IEEE/CVF Conference on Computer Vision and Pattern Recognition*, pages 19647–19656, 2024. 3
- [31] Fusang Wang, Arnaud Louys, Nathan Piasco, Moussab Bennehar, Luis Roldão, and Dzmitry Tsishkou. Planerf: Svd unsupervised 3d plane regularization for nerf large-scale urban scene reconstruction. In *3DV*, 2024. 2, 5
- [32] Jiepeng Wang, Peng Wang, Xiaoxiao Long, Christian Theobalt, Taku Komura, Lingjie Liu, and Wenping Wang. Neuris: Neural reconstruction of indoor scenes using normal priors. In *Computer Vision—ECCV 2022: 17th European Conference, Tel Aviv, Israel, October 23–27, 2022, Proceedings, Part XXXII*, pages 139–155. Springer, 2022. 2
- [33] Peng Wang, Lingjie Liu, Yuan Liu, Christian Theobalt, Taku Komura, and Wenping Wang. Neus: Learning neural implicit surfaces by volume rendering for multi-view reconstruction. In *NeurIPS*, 2021. 2, 4
- [34] Yiming Wang, Qin Han, Marc Habermann, Kostas Daniilidis, Christian Theobalt, and Lingjie Liu. Neus2: Fast learning of neural implicit surfaces for multi-view reconstruction. In *ICCV*, 2023. 2
- [35] Yifan Wang, Di Huang, Weicai Ye, Guofeng Zhang, Wanli Ouyang, and Tong He. Neurodin: A two-stage framework for high-fidelity neural surface reconstruction. *arXiv preprint arXiv:2408.10178*, 2024. 2, 6
- [36] Yida Wang, David Joseph Tan, Nassir Navab, and Federico Tombari. Raneus: Ray-adaptive neural surface reconstruction. In *2024 International Conference on 3D Vision (3DV)*, pages 53–63. IEEE, 2024. 5
- [37] Zian Wang, Tianchang Shen, Jun Gao, Shengyu Huang, Jacob Munkberg, Jon Hasselgren, Zan Gojcic, Wenzheng Chen, and Sanja Fidler. Neural fields meet explicit geometric representation for inverse rendering of urban scenes. In *CVPR*, 2023. 1, 2
- [38] Zian Wang, Tianchang Shen, Merlin Nimier-David, Nicholas Sharp, Jun Gao, Alexander Keller, Sanja Fidler, Thomas Müller, and Zan Gojcic. Adaptive shells for efficient neural radiance field rendering. In *SIGGRAPH Asia*, 2023. 3, 5
- [39] Pengchuan Xiao, Zhenlei Shao, Steven Hao, Zishuo Zhang, Xiaolin Chai, Judy Jiao, Zesong Li, Jian Wu, Kai Sun, Kun Jiang, et al. Pandaset: Advanced sensor suite dataset for autonomous driving. In *ITSC*, 2021. 2, 6, 7, 1, 3
- [40] Lior Yariv, Jiatao Gu, Yoni Kasten, and Yaron Lipman. Volume rendering of neural implicit surfaces. In *NeurIPS*, 2021. 2, 4
- [41] Zehao Yu, Songyou Peng, Michael Niemeyer, Torsten Sattler, and Andreas Geiger. Monosdf: Exploring monocular geometric cues for neural implicit surface reconstruction. *NeurIPS*, 2022. 2
- [42] Zehao Yu, Torsten Sattler, and Andreas Geiger. Gaussian opacity fields: Efficient and compact surface reconstruction in unbounded scenes. *arXiv preprint arXiv:2404.10772*, 2024. 1, 2, 6, 7, 8, 3, 4